



**HAL**  
open science

## An acoustic investigation of the near-surface turbulence on Mars

Baptiste Chide, Philippe Blanc-Benon, Tanguy Bertrand, Xavier Jacob,  
Jérémie Lasue, Ralph D Lorenz, Franck Montmessin, Naomi Murdoch, Jorge  
Pla-Garcia, Fabian Seel, et al.

► **To cite this version:**

Baptiste Chide, Philippe Blanc-Benon, Tanguy Bertrand, Xavier Jacob, Jérémie Lasue, et al.. An acoustic investigation of the near-surface turbulence on Mars. *Journal of the Acoustical Society of America*, 2024, 155, pp.420 - 435. 10.1121/10.0024347 . insu-04413922

**HAL Id: insu-04413922**

**<https://insu.hal.science/insu-04413922>**











Submitted on 24 Jan 2024

**HAL** is a multi-disciplinary open access archive for the deposit and dissemination of scientific research documents, whether they are published or not. The documents may come from teaching and research institutions in France or abroad, or from public or private research centers.

L'archive ouverte pluridisciplinaire **HAL**, est destinée au dépôt et à la diffusion de documents scientifiques de niveau recherche, publiés ou non, émanant des établissements d'enseignement et de recherche français ou étrangers, des laboratoires publics ou privés.

JANUARY 19 2024

## An acoustic investigation of the near-surface turbulence on Mars

Baptiste Chide ; Philippe Blanc-Benon ; Tanguy Bertrand; Xavier Jacob; Jérémie Lasue; Ralph D. Lorenz ; Franck Montmessin ; Naomi Murdoch ; Jorge Pla-Garcia ; Fabian Seel ; Susanne Schröder; Alexander E. Stott ; Manuel de la Torre Juarez ; Roger C. Wiens 



*J. Acoust. Soc. Am.* 155, 420–435 (2024)

<https://doi.org/10.1121/10.0024347>



CrossMark













 **ASA**

Advance your science and career as a member of the  
**Acoustical Society of America**

[LEARN MORE](#)

## An acoustic investigation of the near-surface turbulence on Mars

Baptiste Chide,<sup>1,a)</sup>  Philippe Blanc-Benon,<sup>2</sup>  Tanguy Bertrand,<sup>3</sup> Xavier Jacob,<sup>4</sup> Jérémie Lasue,<sup>5</sup> Ralph D. Lorenz,<sup>6</sup>  Franck Montmessin,<sup>7</sup>  Naomi Murdoch,<sup>8</sup>  Jorge Pla-Garcia,<sup>9</sup>  Fabian Seel,<sup>10</sup>  Susanne Schröder,<sup>10</sup> Alexander E. Stott,<sup>8</sup>  Manuel de la Torre Juarez,<sup>11</sup>  and Roger C. Wiens<sup>12</sup> 

<sup>1</sup>Space and Planetary Exploration Team, Los Alamos National Laboratory, Los Alamos, New Mexico 87545, USA

<sup>2</sup>Laboratoire de Mécanique des Fluides et d'Acoustique, Centre National de la Recherche Scientifique, Ecole Centrale de Lyon, Institut National des sciences appliquées Lyon, Université Lyon 1, Ecully, France

<sup>3</sup>Laboratoire d'études spatiales et d'instrumentation en astrophysique, Observatoire de Paris, Université Paris Sciences & Lettres, Sorbonne Université, Centre National de la Recherche Scientifique, Meudon, France

<sup>4</sup>Institut de Mécanique des Fluides de Toulouse, Université Toulouse 3, Institut National Polytechnique, Centre National de la Recherche Scientifique, Toulouse, France

<sup>5</sup>Institut de Recherche en Astrophysique et Planétologie, Université Toulouse 3, Centre National de la Recherche Scientifique, Centre National d'Etudes Spatiales, Toulouse, France

<sup>6</sup>Space Exploration Sector, Johns Hopkins Applied Physics Laboratory, Laurel, Maryland 20723, USA

<sup>7</sup>Laboratoire Atmosphères Observations Spatiales, Centre National de la Recherche Scientifique, Université Saint-Quentin-en-Yvelines, Sorbonne Université, Guyancourt, France

<sup>8</sup>Institut Supérieur de l'Aéronautique et de l'Espace, Université de Toulouse, Toulouse, France

<sup>9</sup>Centro de Astrobiología, Madrid, Spain

<sup>10</sup>Institute of Optical Sensor Systems, German Aerospace Center, Berlin, Germany

<sup>11</sup>Jet Propulsion Laboratory, California Institute of Technology, Pasadena, California 91109, USA

<sup>12</sup>Department of Earth, Atmospheric, and Planetary Sciences, Purdue University, West Lafayette, Indiana 47907, USA

### ABSTRACT:

The Perseverance rover is carrying out an original acoustic experiment on Mars: the SuperCam microphone records the spherical acoustic waves generated by laser sparks at distances from 2 m to more than 8 m. These  $N$ -shaped acoustic waves scatter from the multiple local heterogeneities of the turbulent atmosphere. Therefore, large and random fluctuations of sound travel time and intensity develop as the waves cross the medium. The variances of the travel times and the scintillation index (normalized variance of the sound intensity) are studied within the mathematical formalism of the propagation of spherical acoustic waves through thermal turbulence to infer statistical properties of the Mars atmospheric temperature fluctuation field. The comparison with the theory is made by simplifying assumptions that do not include wind fluctuations and diffraction effects. Two Earth years (about one Martian year) of observations acquired during the maximum convective period (10:00–14:00 Mars local time) show a good agreement between the dataset and the formalism: the travel time variance diverges from the linear Chernov solution exactly where the density of occurrence of the first caustic reaches its maximum. Moreover, on average, waves travel faster than the mean speed of sound due to a fast path effect, which is also observed on Earth. To account for the distribution of turbulent eddies, several power spectra are tested and the best match to observation is obtained with a generalized von Karman spectrum with a shallower slope than the Kolmogorov cascade,  $\phi(k) \propto (1 + k^2 L^2)^{-4/3}$ . It is associated with an outer scale of turbulence,  $L$ , of 11 cm at 2 m above the surface and a standard deviation of 6 K over 9 s for the temperature. These near-surface atmospheric properties are consistent with a weak to moderate wave scattering regime around noon with little saturation. Overall, this study presents an innovative and promising methodology to probe the near-surface atmospheric turbulence on Mars.

© 2024 Author(s). All article content, except where otherwise noted, is licensed under a Creative Commons Attribution (CC BY) license (<http://creativecommons.org/licenses/by/4.0/>). <https://doi.org/10.1121/10.0024347>

(Received 4 October 2023; revised 13 December 2023; accepted 14 December 2023; published online 19 January 2024)

[Editor: Xun Huang]

Pages: 420–435

### I. INTRODUCTION

Turbulence within the lower atmosphere of Mars, which is in direct contact with the surface (namely, the

atmospheric surface layer), is a critical process as it drives the transport of heat, dust, and trace gases, all of which have a global impact on the overall dynamics of the atmosphere (Petrosyan *et al.*, 2011; Read *et al.*, 2017). Detailed knowledge of the turbulent processes on all spatial and time scales is, therefore, key to understanding the whole climate system

<sup>a)</sup>Email: bchide@lanl.gov

of Mars. On a diurnal time scale, the atmospheric surface layer of Mars is prone to large thermal gradients that generate a strong convection-driven turbulence during the daytime, leading to large temperature fluctuations compared to its counterpart on Earth (Chide *et al.*, 2022; de la Torre Juárez *et al.*, 2023; Munguira *et al.*, 2023). At night, the thermal inversion inhibits the convection, but it may be replaced by shear-induced turbulence at some specific locations and seasons (Chatain *et al.*, 2021; Pla-García *et al.*, 2023). The current understanding of small scale processes, especially the turbulence energy cascade, relies on terrestrial-based models that have been adapted for Mars. Therefore, *in situ* observations are crucial to validate such models. These small scale processes have been described by the Insight mission in terms of pressure fluctuations up to 2 Hz (Banfield *et al.*, 2020; Temel *et al.*, 2022), but no data at higher frequency exist due to the lack of suitable sensors. Moreover, such small scales cannot be resolved by atmospheric models, e.g., large eddy simulations, and are instead parameterized in the latter example. Indeed, *in situ* observations of the atmospheric boundary layer processes are crucial for testing large eddy simulations predictions, which sometimes include different small scale diffusion and turbulent scheme, yielding very different predictions (Bertrand *et al.*, 2016).

The random inhomogeneities in a turbulent atmosphere are known to greatly affect sound propagation by scattering the phase and amplitude of acoustic waves. The statistics of these scattering properties has been extensively described by theoretical (Ishimaru, 1997; Tatarskii, 1967) and experimental works (Blanc-Benon and Juvé, 1993). The resulting mathematical formalism has been used to describe the distribution of the turbulent scales in the Earth's atmospheric layer (Wilson *et al.*, 1999). Here, the objective of this paper is to test if this formalism can be applied to data obtained on Mars and, for the first time, to infer small scale properties of its atmospheric surface layer turbulence.

The NASA Perseverance rover, which landed on Mars on February 18, 2021 (Farley *et al.*, 2020), offers a unique combination of a microphone and controlled sound source at various distances (Maurice *et al.*, 2022). The microphone of the SuperCam instrument (Maurice *et al.*, 2021; Mimoun *et al.*, 2023) records the Mars soundscape for the first time between 20 Hz and 50 kHz, as well as artificial sounds produced by the rover and its equipment. Since landing, several results have been published (Chide *et al.*, 2022; Lorenz *et al.*, 2023; Murdoch *et al.*, 2022; Stott *et al.*, 2023), highlighting the great potential of acoustic investigations for Mars. The main artificial sound source recorded by the microphone is created by the SuperCam pulsed laser, which vaporizes a few nanograms of matter at the surface, and subsequently generates a plasma that extends to several millimeter in size (Vogt *et al.*, 2022). The optical spectrum from this plasma is used to measure the elemental composition of the targeted rocks and soils with an analytical method laser-induced breakdown spectroscopy (Maurice *et al.*, 2021; Wiens *et al.*, 2020). As the plasma expands in Mars' atmosphere, it generates a shockwave (Seel *et al.*, 2023) that results in an  $N$ -shaped acoustic wave

(2–25 kHz), which can be recorded by the microphone. The absolute amplitude of this pressure signal has been used to characterize the unique sound propagation properties of the low-pressure CO<sub>2</sub>-dominated Mars atmosphere, i.e., large sound absorption and seasonal variation of the acoustic impedance (Chide *et al.*, 2023). However, these laser sparks are produced and recorded at a fast cadence of 3 Hz over 10 s, which is reminiscent of laboratory experiments designed to study the propagation of spherical waves through turbulent medium (Averiyanov *et al.*, 2011; Yuldashev *et al.*, 2017). Therefore, the analysis presented here focuses on the variance of the amplitude and travel time of these acoustic waves induced by thermal fluctuations to statistically characterize the near-surface turbulence using the acoustic formalism (Blanc-Benon and Juvé, 1993).

This is the first acoustic experiment ever performed on Mars and for which, unfortunately, experimental parameters are not as controlled as they would be in laboratory experiments. In this context, we have considered the following approximations: we place ourselves in the framework of geometric acoustics, which means that diffraction effects are neglected. Second, we only consider temperature fluctuations, and wind velocity fluctuations are ignored. Furthermore, we assume that temperature fluctuations do not depend on the height over the first 2 m above the ground, where the experiment is performed. All these hypotheses are discussed in the text and could be explored and refined in future research.

The geometry of the experiment, the dataset considered, and the quantities used [travel time and scintillation index (SI)] are presented in Sec. II, along with a discussion on the validity of this experiment with regard to the various lengths and time scales. Then, Sec. III is devoted to the study of travel times and testing various turbulence models that can account for the nonlinear behavior of travel times with distance. Section IV deals with acoustic scintillation to discriminate which of the turbulence models tested represents the Mars data the best. In short, a power spectrum for the eddy size distribution, their characteristic scales, and the associated temperature fluctuations are proposed to describe the turbulence around noon local time.

## II. AN ACOUSTIC EXPERIMENT ON MARS

The laser and microphone are mounted at about 2.1 m above the ground (Fig. 1). The longitudinal axis,  $z$  axis, connects the target to the microphone. The plasma is at  $z=0$  and the microphone is at  $z=x$ , which represents the propagation distance. Because the laser is focused onto targets at various distances from the rover for sample analysis, the propagation distance varies from target to target. Note that for each target, there is a different  $z$  axis as targets are located at different distances from the rover.

### A. Mars dataset

The dataset consists of data acquired by SuperCam at the top of Perseverance rover mast over the first 800 Sols (Martian solar day; 1 Sol = 88 775 s; Sol 0 is the landing

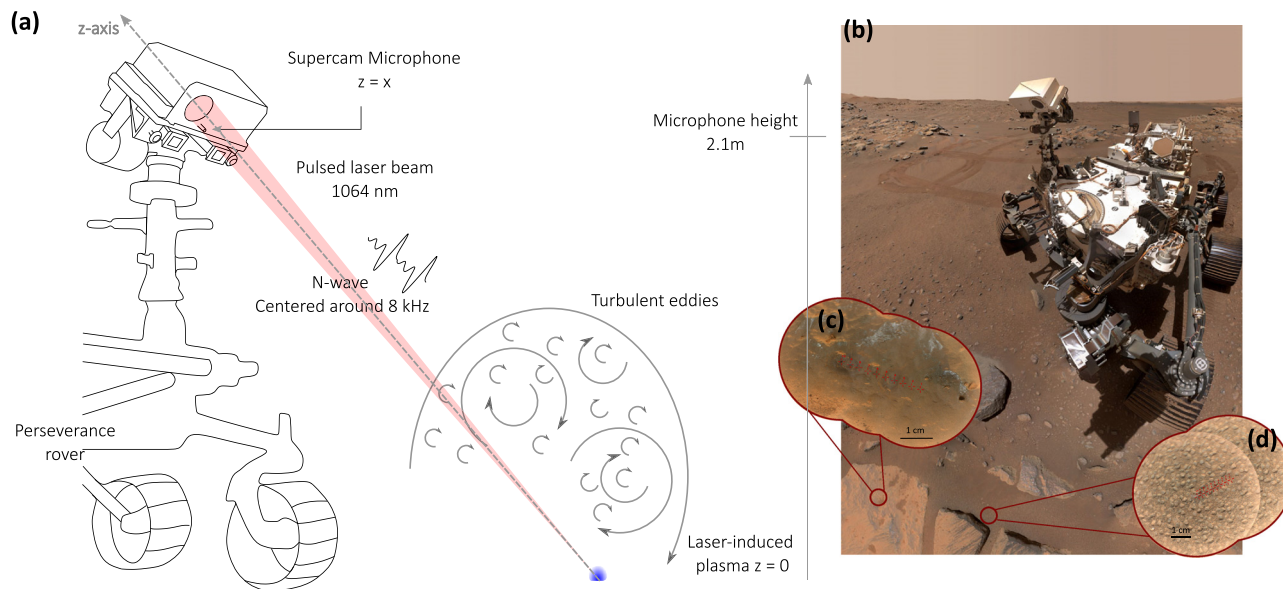


FIG. 1. (Color online) (a) Geometry of the SuperCam microphone recordings of the laser-induced-acoustic signal, where the propagation path (2–11 m) goes through the thermal turbulence generated in the atmospheric surface layer of Mars. (b) View of the Perseverance rover on Mars (Credits: NASA/JPL-Caltech/MSSS). (c) Context image of a SuperCam raster on rock target Grandes Tours du Lac (Sol 181, 10 points, 30 laser shots each) and (d) soil target Chambares (Sol 185, 10 points, 50 laser shots each) are shown. Credits for (c) and (d): NASA/JPL-Caltech/LANL/CNES/IRAP.

day, February 18, 2021) of the Mars 2020 mission (Farley *et al.*, 2022). Acoustic data closer than 2 m and farther than 8 m were removed: data closer than 2 m corresponds to the on board calibration targets at the rear of the rover and result in a different propagation path above the artificially heated rover deck. Targets farther than 8 m were also discarded because their signal-to-noise ratio of the associated audio signal is lower than two.

Acoustic recordings are performed at 100 ksamples/s (Mimoun *et al.*, 2023). Although the microphone bandwidth starts at 20 Hz, laser-induced electromagnetic interference associated with subsystem heating dominates signals below 1 kHz (Maurice *et al.*, 2021). However, 95% of the acoustic energy produced by a laser-induced spark is between 2 and 15 kHz (Maurice *et al.*, 2022). Therefore, the instrument limitation below 1 kHz is of no consequence for the current investigation.

SuperCam operates the laser at a repetition rate of 3 Hz by bursts of 30 shots, 29 of which are recorded by the microphone (the 30th shot is not recorded). For a surface target, such a sequence is usually repeated 5–10 times on fresh sampling points separated by a few millimeters. Per burst, the first three shots are discarded because they are potentially affected by dust on the surface (Lasue *et al.*, 2018). Therefore, a series of 26 shots per burst is used and recorded in less than 9 s. Occasionally, there are bursts of 125 shots (or 150 shots) to penetrate deeper into the rocks. These bursts are separated into data packets of 29 shots before applying the process above.

To support chemistry data, SuperCam acquires high resolution images of each target sampled by the laser. These images provide geological context for the geochemical analysis and interpretation. Manual classification of those

images for this study results in three categories: rocks, the vast majority of the targets that are hard natural surfaces on the ground; soils, for unconsolidated targets, including regolith and drill tailings; drill holes, a few attempts to shoot inside rover’s drilled holes. However, because of a very particular geometry that induces a lot of echoes, shots inside drill holes are discarded.

Finally, to consolidate the dataset, some recordings have been discarded when the focus of the laser is known to be bad or the determination of the *N*-wave arrival time is ambiguous. On the contrary, windy recordings are not rejected even when wind noise is detected in the time series. Note that distances are not evenly distributed: targets at close distances are investigated more often than those at long distance. Hence, 50% of the rock targets are between 2 and 2.8 m. Targets are sampled during the daytime from 07:06 to 19:07 local true solar time (LTST), and 70% of the recordings are acquired between 10:00 and 14:00 LTST because of operational constraints. This time period also corresponds to the maximum of turbulence intensity during a Sol. Therefore, unless mentioned otherwise, most of this study is based on data collected between 10:00 and 14:00 LTST to maintain a similar turbulence level. In total, this dataset relies on 70 000+ recordings, assembled as 2762 consecutive sets of 26 recordings (13% are soils and 77% are rocks), corresponding to 262 different targets sampled between 2 and 8 m.

## B. Acoustic signal

When the laser pulse hits the target with an irradiance greater than  $1 \text{ GW cm}^{-2}$ , it vaporizes a few nanograms of matter, which subsequently becomes a plasma. The plasma expands at supersonic speed into the ambient atmosphere,

creating a shock wave. Its speed quickly decays to the local speed of sound and propagates as an  $N$ -wave (Chen *et al.*, 2000).

The acoustic recordings of the  $N$ -waves cover 60 ms around each laser pulse. The start of the recording window is precisely triggered on the laser ignition. The time for the laser beam to hit the target is negligible. First, the plasma expansion is supersonic: after about  $23 \mu\text{s}$ , the pressure wave reaches the speed of sound; 15 mm have been covered at an average speed of  $714 \text{ ms}^{-1}$  (Seel *et al.*, 2023), i.e., about three times the sound speed, which is about  $255 \text{ ms}^{-1}$ . The travel time is given by the rise of the pressure wave since the laser was fired minus  $23 \mu\text{s}$  as we only consider the sonic propagation. Because of the uncertainty on the travel time detection, we estimate the global error on the propagation time to be  $10 \mu\text{s}$ . Over bursts of 26 recordings, the quantities that are measured in this study are the mean travel time,  $\langle \delta t \rangle$ , and the variance of the travel time,  $\sigma_t^2 = \langle (\delta t - \langle \delta t \rangle)^2 \rangle$ . For  $x = 2, 4,$  and  $6 \text{ m}$ ,  $\langle \delta t \rangle \simeq 7.8, 15.6,$  and  $23.5 \text{ ms}$ , respectively. For the same distances,  $\sigma_t^2 \simeq 2 \times 10^{-9} \text{ s}^2, 6 \times 10^{-9} \text{ s}^2,$  and  $13 \times 10^{-9} \text{ s}^2$ , respectively.

The amplitude of the acoustic signal,  $p$ , in Pa, also referred to as the pressure, is given by the first maximum of the  $N$ -wave (compression wave).  $p$  decreases along its propagation path because of the geometric spreading of the spherical wavefront (as the inverse of  $x$ ) and the energy exchanges with molecules of the atmosphere (Chide *et al.*, 2023). For  $x = 2, 4,$  and  $6 \text{ m}$ ,  $p \simeq 354, 76,$  and  $16 \text{ mPa}$ , respectively. As such, the absolute value of the pressure is not used because it depends on other multiplicative factors on top of geometric spreading and absorption, which are mentioned above: quality of the focus, thermal dissipation of the ablated surface, and hardness of the rock (Chide *et al.*, 2020). Instead, the normalized variance of the signal intensity is used. By analogy with optics, this is called the scintillation index, SI, a value that is employed to characterize the fluctuations of an optical wave when propagating through atmospheric turbulence (Hill and Frehlich, 1996) or for underwater acoustics (Cotté *et al.*, 2007). This index has been used by Blanc-Benon and Juvé (1993) to support laboratory experiments of thermal-induced turbulence. SI is defined as the variance of the sound intensity divided by the square of the mean sound intensity, where the mean is over the 26 shots used at each observation point, and the variance is determined per point such that each observation point has a defined SI value. As the sound intensity,  $I$ , is proportional to the square of the pressure, SI can also be written as the fourth moment of the pressure, which is directly measured by the microphone,

$$SI = \frac{\langle (I - \langle I \rangle)^2 \rangle}{\langle I \rangle^2} = \frac{\langle p^4 \rangle - \langle p^2 \rangle^2}{\langle p^2 \rangle^2}. \quad (1)$$

Figure 2(a) shows SI values for the different populations of our dataset at all local times. For rocks, SI values in the range 0.002–3. Soils show a wider range of SI values, particularly high, up to ten. Indeed, the laser-induced

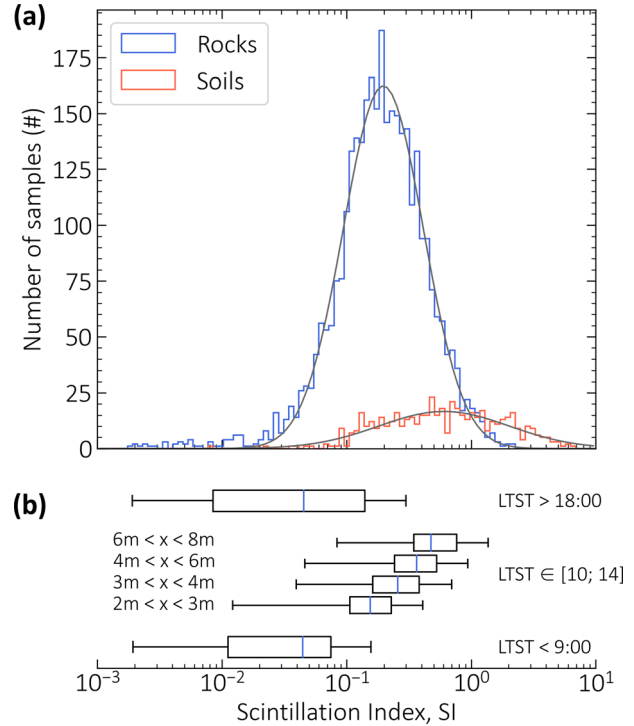


FIG. 2. (Color online) Distribution of SI values, showing (a) histogram for rocks (blue) and soils (red) at all local times. Each population is fitted by a lognormal distribution. (b) Box plots (minimum, first quartile, median, third quartile, and maximum) for SI on rocks at three local times:  $<9:00$ , between  $10:00$  and  $14:00$ , and  $>16:00$  LTST. For the midday period, box plots are subdivided into four distance ranges to targets on the ground, whereas for the morning and evening periods, they include data from 2 to 8 m.

acoustic signal in soils decreases drastically over 26 shots because of the formation of a several millimeter deep pits in such a loose material (Alvarez-Llamas *et al.*, 2023). This adds another source of variability in the shot-to-shot acoustic signal and explains the higher values. For this reason, the soil population is excluded for the remainder of the study. SI values on rocks also depend on distance and local time as depicted in Fig. 2(b). This behavior is consistent with the idea developed in Sec. IV. SI is driven by turbulence; SI values are low at dusk and dawn and large at midday. It follows the diurnal evolution of the turbulence on Mars: a strong turbulence during the daytime and a more stratified atmosphere during the nighttime (Spiga, 2019). Moreover, SI increases with distance: the farther away the targets are, the more turbulence cells the acoustic wave goes through, and the more variability is created.

To describe the propagation of acoustic waves through a turbulent medium, the log of the acoustic amplitude,  $\chi$ , is also used and, particularly, its variance:  $\sigma_\chi^2$  (Tatarskii, 1961). Like SI,  $\sigma_\chi^2$  is independent of the absolute amplitude of the pressure, making it an easy-to-handle quantity.

### C. Validity of the experiment

To be sure of the validity of this acoustic experiment on Mars over 9 s (i.e., the duration of 26 shots at 3 Hz), three

conditions need to be verified over this time scale: (i) the laser energy is stable, (ii) the laser beam itself is not disturbed by atmospheric turbulence, and (iii) the turbulence scales are small compared to the characteristic scale of the experiment and large compared to the acoustic wavelength.

- (i) Shot-to-shot variations of the laser energy over a burst induce variations of the irradiance on target, which create an acoustic scintillation that does not depend on turbulence. Laboratory experiments over 30 shots have demonstrated that the laser energy is stable at 3% root mean square (RMS; Maurice *et al.*, 2021), which gives  $SI \sim 10^{-3}$ . This can be observed as a noise floor for the significance of SI. Measured values of SI are above this threshold (Fig. 2);
- (ii) atmospheric turbulence will affect the propagation of the laser beam between the microphone and targets on the ground: it causes local variations in the refractive index, which, in turn, induces scintillation of the laser beam itself if the turbulence is strong enough. For the sake of brevity, this discussion is deferred to Appendix A. There, it is verified that within the limits of this experiment, the most extreme atmospheric turbulence produces a scintillation  $SI < 10^{-3}$  of the laser for targets between 2 and 8 m. This is below what is measured on Mars for acoustic scintillation (see Fig. 2). The Mars' atmosphere is not dense enough; and
- (iii) the theory of wave propagation in turbulent media, to which we will refer, is founded on the statistical representation of random media (Iooss *et al.*, 2000). To make the statistical inference possible, waves must traverse several heterogeneities along their propagation path. It will be revealed later that the turbulence scale is  $L \simeq 11$  cm. Propagation lengths between 2 and 8 m are 20–70 times the characteristic scale of the turbulence. The same theory uses the parabolic approximation to connect fluctuations of a spherical wave to the variations of the medium of propagation. This approximation is valid if the dominant wavelength,  $\lambda$ , is shorter than the size of the heterogeneities (Rytov *et al.*, 1987). Indeed, at 8 kHz,  $\lambda$  is about 3 cm and, therefore, is smaller than  $L$ .

In conclusion, the different length scales, aided by the low density of the Martian atmosphere and the stability of the setup, make the value of SI meaningful. The only limitation is given by the inclined geometry (Fig. 1), which would not be used in a laboratory experiment: the laser shoots downward, and it can be imagined that the distribution of turbulent structures along the propagation path is not homogeneous (Martins *et al.*, 2021).

### III. TRAVEL TIMES

In this section, the dataset is restricted to recordings performed between 10:00 and 14:00 LTST such that it consists of waves that have propagated in similar turbulent conditions (still 70% of the data).

### A. Fluctuation field

Along the propagation path ( $z$  axis) at a distance  $x$  from the source, the acoustic wave encounters varying speeds of sound,  $c(x)$ , around a mean value,  $c_0$ . Fluctuations of the speed of sound induce fluctuations of the travel times. Speed of sound and travel time are related through the Eikonal equation:

$$|\nabla \delta t(x)|^2 = \frac{1}{c(x)^2} = \frac{1}{c_0^2} (1 + \epsilon(x)). \quad (2)$$

It is assumed that  $\epsilon$  is a weak and centered random temperature fluctuation field:  $|\epsilon| \ll 1$  and  $\langle \epsilon \rangle = 0$ . It is related to the variations of the speed of sound through the right side of Eq. (2). Furthermore, it is assumed that  $\epsilon$  is statistically homogeneous and the medium is isotropic. Then, the field,  $\epsilon$ , is defined by its covariance function such that

$$C_\epsilon(x) = \sigma_\epsilon^2 N \left( \frac{x}{L} \right). \quad (3)$$

The scale,  $L$ , is defined as the outer scale of turbulence, i.e., the characteristic size of the largest turbulent eddies, which is also referred to as the energy production scale. It corresponds to the beginning of the inertial regime. The field strength is defined by its variance,  $\sigma_\epsilon^2$ , and its standardized covariance,  $N$ . Although  $L$  and  $\sigma_\epsilon^2$  are expected to vary with the height above the ground following the Monin-Obukhov similarity theory (Petrosyan *et al.*, 2011), here, these parameters are assumed to be constant.

In this study, different representations of the perturbation field, i.e., the distribution of the turbulent feature sizes, are tested. They are represented by their power density spectrum,  $\phi(k)$ , as a function of the wavenumber  $k$  (see Fig. 3):

- Gaussian field:  $\phi(k) \propto \exp(-k^2 L^2)$ ;
- pure Kolmogorov field:  $\phi(k) \propto (k^2 L^2)^{-11/6}$ ; and
- generalized von Karman field:  $\phi(k) \propto (1 + k^2 L^2)^{-p-3/2}$ , where  $p$  is a parameter. Note that when  $p = 1/3$ , it is commonly referred as the von Karman spectrum.

For large wavenumbers, i.e., for very small eddies, viscous effects become important and the energy is dissipated. This viscous dissipation range begins for eddies smaller than the inner scale of turbulence,  $l_0$ . To take into account the dissipation of energy at large wavenumbers, the generalized von Karman field is modified by an  $\exp(-k^2 l_0^2)$  term that marks the end of the inertial regime. For Mars, it is assumed that  $l_0 = 0.02$  m (Maurice *et al.*, 2022; Petrosyan *et al.*, 2011), but this value may vary with the time of the day and season. In this study, this modified von Karman spectrum is not considered.

The Gaussian field drops very fast with the wavenumber,  $k$ . The pure Kolmogorov spectrum decays less rapidly with the wavenumber than the Gaussian field. However, it has no finite bound for low  $k$  values. Then, a more sophisticated shape is the generalized von Karman spectrum, which is defined beyond the outer scale of turbulence,  $L$ , with a shallower slope than that for the Gaussian field. This is more

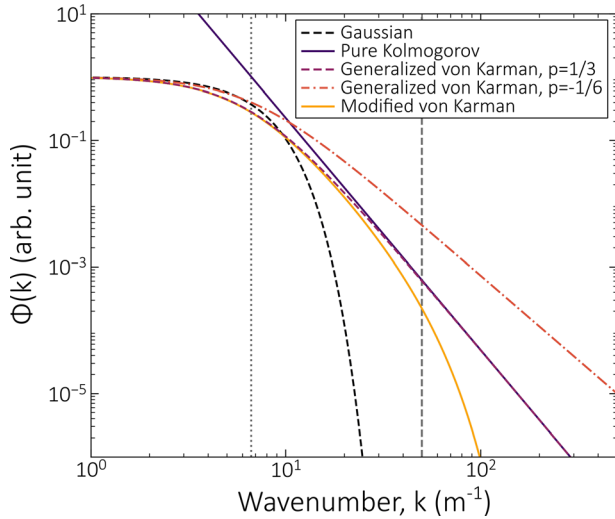


FIG. 3. (Color online) Power spectra (vertical scale is arbitrary) of the different turbulence models tested in this study. They are built using an outer scale of turbulence,  $L = 0.15$  m. For the modified von Karman spectrum with dissipation, the inner scale,  $l_0$ , is  $0.02$  m. At low wavenumbers, the generalized von Karman spectrum with  $p = 1/3$  (dashed violet) superimposes with the von Karman spectrum modified with dissipation (solid yellow), whereas at large wavenumbers, it superimposes with the pure Kolmogorov spectrum (solid purple). Wavenumbers associated with  $L$  and  $l_0$  are indicated with gray dotted and dashed vertical lines, respectively.

realistic as it converges to a pure Kolmogorov shape for large values of  $k$  and reaches a plateau at low values of  $k$ . This spectrum is the first to come to mind to describe the planetary surface layer (Kaimal *et al.*, 1972).

In the geometrical optics for a three-dimensional (3D) spherical wave, Iooss *et al.* (2000) found that for targets at different distances,  $x$ , the mean travel time,  $\langle \delta t \rangle$ , and its variance,  $\sigma_t^2$ , can be written as

$$\langle \delta t \rangle = \frac{x}{c_0} + \frac{A_2 \sigma_\epsilon^2 x^2}{24 c_0 L}, \tag{4}$$

$$\sigma_t^2 = \frac{A_1 \sigma_\epsilon^2}{2 c_0^2} Lx + \frac{A_2^2 \sigma_\epsilon^4 x^4}{288 c_0^2 L^2}. \tag{5}$$

The first term in Eq. (4) is the mean travel time for a constant speed along the propagation path. At first order, the variations of the mean travel time are zero as  $\langle \epsilon \rangle = 0$ . The second order takes into account the perturbations that accelerate or decelerate the wave. The first term of Eq. (5) is a well-known result and called the Chernov model (Chernov *et al.*, 1960; Obukhov, 1994). It gives the first-order fluctuations by integrating the perturbations along the straight ray. The second term is calculated by Iooss *et al.* (2000), and it describes the effect of the ray bending caused by the perturbations. When ray bending increases, stronger nonlinear travel time perturbations appear. The parameters  $A_1$  and  $A_2$  are given by the covariance structure  $N$  (see Appendix B), which depends on the field distribution considered.

**B. Gaussian field**

To start this study, let us assume the simplest perturbation field and that  $\epsilon$  is Gaussian in all directions, i.e., fluctuations are

very smoothed. Such a distribution is given by only one scale of inhomogeneity: the outer scale of turbulence,  $L_{\text{Gauss}}$ . Then, the spectral density is  $\phi(k) \propto \exp(-k^2 L_{\text{Gauss}}^2)$  and the Gaussian covariance is  $N(u) = \exp(-u^2)$ . It is found that  $A_1 = \frac{1}{2} \pi$  and  $A_2 = -\sqrt{\pi}$  (see the details in Appendix B).

First, the variance of travel time is examined. Figure 4 shows the application of this Gaussian model to this Mars dataset. At first order, the variance of the travel time follows the quadratic trend expected from Eq. (5). Considering  $c_0 = 254.9 \pm 0.1 \text{ ms}^{-1}$  (see later in Fig. 5) in the case of the Gaussian model, the fit of Eq. (5) to the data leads to a first characterization of the fluctuation field,  $\epsilon$ : the typical size of the turbulent eddies is  $L_{\text{Gauss}} = 14 \pm 1 \text{ cm}$  ( $\pm 1\sigma$ ) and  $\sigma_\epsilon^2 = 7.4 \cdot 10^{-4} \pm 0.7 \cdot 10^{-4}$  ( $\pm 1\sigma$ ). Still, a significant scattering is observed in Fig. 4, which might be attributed to non-negligible diffraction effects. Indeed, Eq. (5) is valid in the geometrical acoustics approximation (Iooss *et al.*, 2000), which is valid when the wave parameter  $D = x / (k L_{\text{Gauss}}^2)$  (Ostashev and Wilson, 2017) is much lower than one. Here,  $D$  is lower than one for  $x$  closer than 4 m (the majority of our dataset) and is no higher than four for 8 m. Therefore, this experiment might be at the limit of the weak diffraction regime ( $D \ll 1$ ), especially for longer propagation distances. It is also consistent with the fully saturated scattering regime of the acoustic wave at such distances (see Fig. 6). Moreover, data from targets beyond 7 m seem to deviate from the fitted solution. Actually, Eq. (5) is valid if the second term is relatively small compared to the first term (Iooss *et al.*, 2000). Or, for distances longer than 7 m, the quadratic term is more than twice the value of the Chernov model such that it supports that Eq. (5) might be no longer valid at long distances. On the other hand, the scattering of the data

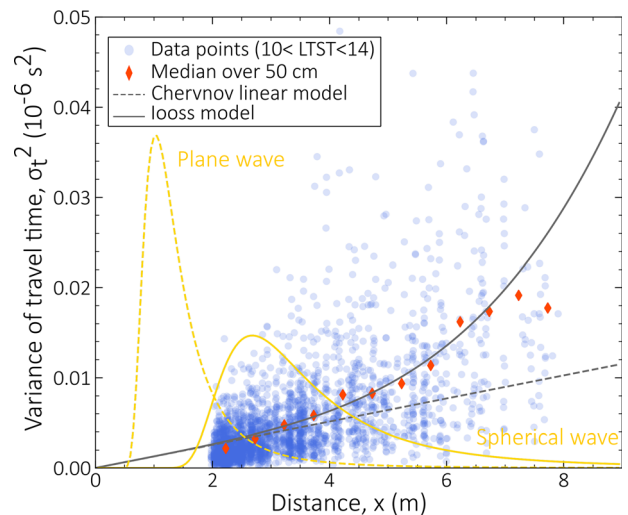


FIG. 4. (Color online) Variance of the travel time,  $\sigma_t^2$ , as a function of the propagation distance,  $x$ . All points between 10:00 and 14:00 LTST are denoted by blue circles, and median over bins of 0.5 m are denoted by red diamonds. The latter are fitted with the model in Eq. (5) (solid gray line). The dashed gray line represents the Chernov linear model [first term in Eq. (5)]. In yellow, note the probability density of occurrence of the first caustic for a plane wave (dashed yellow) and a spherical wave (solid yellow). The relative heights of these two densities are correct, but their amplitude scale units are arbitrary.



points might also be attributed to turbulence characteristics that are not necessarily the same from one recording to the other due to seasonal variations and wind fluctuations, which are not taken into account in this study.

To find the origin of the departure from the linear Chernov model, we look at the probability density of occurrence of the first caustic. It is given by (Blanc-Benon *et al.*, 1995; Iooss *et al.*, 2000; Kulkarny and White, 1982; White, 1984)

$$p(\tau) = \frac{\alpha}{\tau^4} \exp(-\beta/\tau^3), \quad (6)$$

where

$$\tau = \left( \frac{\sqrt{\pi}}{2L_{\text{Gauss}}^3} \sigma_{\epsilon, \text{Gauss}}^2 \right)^{1/3} x.$$

Coefficients  $\alpha = 0.87$  and  $\beta = 0.33$  are calculated for a plane wave. Hence, the probability density has a bell shape, and its center,  $x_{c, \text{plane}}$ , is given by

$$x_{c, \text{plane}} = \left( \frac{3L_{\text{Gauss}}^3}{2\sqrt{\pi}\sigma_{\epsilon, \text{Gauss}}^2} \right)^{1/3} \beta^{1/3}, \quad (7)$$

where the values of  $\sigma_{\epsilon, \text{Gauss}}^2$  and  $L_{\text{Gauss}}$  are given above (Fig. 4), and it gives  $x_{c, \text{plane}} = 1.03$  m. There is no analytical solution for a spherical wave, but Hugon-Jeannin (1992) indicates that the center of the probability density needs to be shifted by a factor of 2.6 for a spherical wave. Thus, a new value,  $\beta = 5.80$ , is determined to match this position of the maximum. A new value,  $\alpha = 15.81$ , is considered to keep the same integral below the probability density, even if it does not matter for this study because the absolute value of the density is not discussed. Hence, a probability density for a spherical wave can be estimated (see Fig. 4). Closer than 1.5 m, the value of the probability is near zero, i.e., no caustic occurs. The maximum is centered at  $x_{c, \text{sphere}} = 2.68$  m, exactly where the variance of travel times diverges from the Chernov linear model. It will extend nearly to the limits of the experiment.

The distribution of mean of travel times with distance given by Eq. (4) is now examined. A precise fit of the second order deviation is not expected as this quantity is close to the 10  $\mu\text{s}$  precision. The first-order fit of the mean travel time as a function of distance (see inset in Fig. 5) gives  $c_0 = 254.9 \pm 0.1 \text{ m}\cdot\text{s}^{-1}$  ( $\pm 1\sigma$ ), which is the value used above as an input for the calculation of  $\sigma_{\epsilon, \text{Gauss}}^2$  and  $L_{\text{Gauss}}$ . Considering an ideal gas, it corresponds to a temperature  $T_0 = 242$  K, which is a value representative of those measured at Jezero crater (Munguira *et al.*, 2023; Rodriguez-Manfredi *et al.*, 2023). As expected, the determination of the time shift,  $\langle \delta t \rangle - x/c_0$ , is poorly constrained (see Fig. 5). However, the data show a negative time shift (i.e., a negative slope in the fit in Fig. 5), which is in agreement with the model predicted by Eq. (4). In fact, acoustic waves favor the shortest path and, therefore, statistically, the effective velocity is higher than the mean velocity of the medium. This is similar to the propagation of light in a medium with varying indices and the choice of the shortest path (Fermat's law).

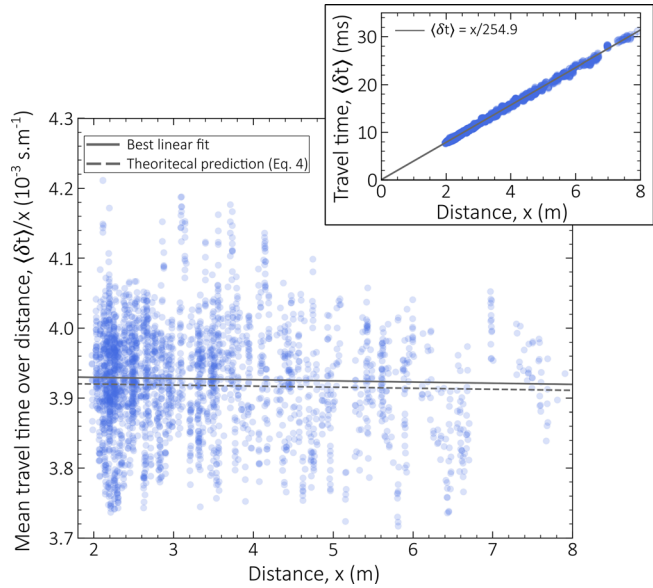


FIG. 5. (Color online) Variation of mean travel time with the propagation distance, showing (inset) mean travel time as a function of the distance and (main plot) mean travel time divided by the distance as a function of the distance. It is fitted with a linear function (solid gray line). This best fit is compared with the theoretical evolution (dashed line) as predicted by Eq. (4), using the parameters determined for a Gaussian field in Sec. III B.

This effect is often called the fast path effect in the literature (Blanc-Benon and Juvé, 1993; Codona *et al.*, 1985): a shorter travel time is expected for unsaturated and partially saturated scattering regime while a pulse delay remains for the fully saturated regime (see Sec. III D). The latter might be observed for distances farther than 7 m, which are likely to fall in the fully saturated regime. However, the dispersion of this dataset does not allow to draw further quantitative conclusions on the fast path effect.

Finally, to relate the fluctuation field,  $\epsilon$ , to temperature variations, the variance of the temperature along the propagation path,  $\sigma_T^2$ , is derived to first order from Eq. (2) and the ideal gas law:

$$\sigma_T^2 = T_0^2 \frac{\sigma_\epsilon^2}{4}. \quad (8)$$

Hence, with  $\sigma_\epsilon^2 = \sigma_{\epsilon, \text{Gauss}}^2 = 7.4 \times 10^{-4}$ , it gives  $\sigma_T = 3$  K, which is  $\pm 1.4\%$  of  $T_0$ . This value is consistent with the fluctuations reported in Jezero (de la Torre Juárez *et al.*, 2023).

### C. Testing non-Gaussian fields

The results above were derived for a Gaussian spectrum. In this section, the other turbulence distributions mentioned above (see Fig. 3) are being tested, with the exception of the pure Kolmogorov spectrum for which the approach of Iooss *et al.* (2000) for the travel times does not work because such a spectrum has no finite bound for low  $k$  values (the coefficients  $A_1$  and  $A_2$  cannot be calculated).

For the generalized von Karman spectrum, coefficients  $A_1$  and  $A_2$  are more difficult to constrain as the spectrum depends on an additional parameter,  $p$ .  $A_1$  and  $A_2$  for the generalized

von Karman spectrum have been calculated in Appendix B. The parameter  $p = 1/3$  leads to the classical  $-11/6$  exponent for a Kolmogorov cascade (Tatarskii, 1961). For such a model of turbulence,  $L_{\text{vKarman},p=1/3} = 1.63 L_{\text{Gauss}}$  and  $\sigma_{\epsilon,\text{vKarman},p=1/3}^2 = 1.28 \sigma_{\epsilon,\text{Gauss}}^2$ . For a shallower spectrum with  $p = -1/6$ , we find that  $L_{\text{vKarman},p=-1/6} = 0.85 L_{\text{Gauss}}$  and  $\sigma_{\epsilon,\text{vKarman},p=-1/6}^2 = 2.7 \sigma_{\epsilon,\text{Gauss}}^2$ . The choice for  $p = -1/6$  is justified later.

Finally, it has to be noticed that Eq. (5) only gives the intensity of the fluctuation field and its characteristic scale for a given distribution. It does not help to constrain which distribution is the most appropriate to describe the Mars atmosphere. Rather, this will be the focus of Sec. IV.

### D. Sound wave scattering

The field characteristics (i.e.,  $L$  and  $\sigma_\epsilon^2$ ) have been derived for the Gaussian and generalized von Karman fields. What does this turbulence field induce in terms of acoustic wave scattering? Experimental points are reported on a dimensionless  $\Lambda - \Phi$  diagram derived by Flatté (1983) from ocean studies.  $\Phi$  is a strength parameter: when  $\Phi$  is large, much greater than one, the turbulence is strong and induces many acoustic paths between the source and microphone, which are, on average, uncorrelated; when  $\Phi$  is small, much lower than one, the propagation approaches only one acoustic path.  $\Lambda$  is a diffraction parameter: when  $\Lambda < 1$ , the geometric approximation is valid, whereas for large values,  $\Lambda > 1$ , diffraction occurs. The combination of these parameters leads to well-defined boundaries between the different scattering regimes: when  $\Lambda\Phi^{2.4} < 1$ , the regime is said to be unsaturated; saturation occurs when  $\Lambda\Phi^{1.2} > 1$ . An intermediate regime lies in between. From Codona et al. (1985), we can work an analogy with ray paths. Unsaturated behavior corresponds to one stationary-phase acoustic path and occurs for weak fluctuations. In a fully saturated behavior situation, the original acoustic path breaks up into many new micropaths, which are statistically independent of each other. Partially saturated behavior occurs in a medium, typically, with a power-law spectrum, which has enough small scale fluctuations to cause the breakup into many micropaths, and enough large-scale fluctuations to make the micropath bundle behave like a single path in its wandering from the unperturbed path (Dashen, 1979). Experiments in waves propagating through continuous random media typically fall into this category. More details on the meaning of  $\Phi$  and  $\Lambda$  can be found, for example, in Karweit et al. (1991) or Cotté et al. (2007). The analytical formulas for these parameters are (Wilson, 2000)

$$\begin{cases} \Phi = \sqrt{2 \mathcal{L} k_0^2 x \langle \mu^2 \rangle}, \\ \Lambda = x / (6k_0 \mathcal{L}^2), \end{cases} \quad (9)$$

where  $k_0$  is the acoustic wave number (defined at 8 kHz),  $x$  is the propagation distance, and  $\mathcal{L}$  is the integral turbulence scale, i.e., the average size of the turbulent eddies, which is

defined as  $\mathcal{L} = 0.74L$  (Cotté et al., 2007).  $\mu$  is the RMS of the sound velocity fluctuations. From Eq. (2), we find that  $\langle \mu^2 \rangle = \sigma_\epsilon^2 / 4$ .

$\Lambda$  and  $\Phi$ , computed for the Gaussian field characteristics and generalized von Karman field characteristics, are projected on a Flatté plot in Fig. 6. As the distance increases, the likelihood of saturation increases. For both models, the acoustic signal is not saturated before 3 m. It is fully saturated beyond 6 m with the Gaussian model hypothesis and beyond 7 m with the generalized von Karman model hypothesis. This is consistent with the deviation of the travel time from the Iooss model in Fig. 4 for distances longer than 7 m. In between, most of the points lie in the partially saturated. Of course, this representation is not definitive as the parameters of the models can vary. However, it allows us to verify that our acoustic experiment on Mars is well sized, coincidentally, to probe the near-surface turbulence of Mars. More can be performed from Flatté theory, in particular, looking back at time series and the shape of  $N$ -waves when the signal is said to be saturated (Yuldashev et al., 2017); this will be the subject of a future study.

### IV. ACOUSTIC SCINTILLATION

The amplitude of the sound pressure wave is now investigated. Figure 7 displays sound amplitude and sound speeds for four 29 shot recordings. The greater the dispersion of the amplitude, the larger the SI value is by definition of SI. As discussed in Chide et al. (2023), this amplitude scattering is attributed to turbulence: the morning recordings [Figs. 7(a) and 7(b)] are more stable, and those around noon [Figs. 7(c) and 7(d)] are much more scattered. For the same local time (i.e., assuming a similar level of turbulence), a longer

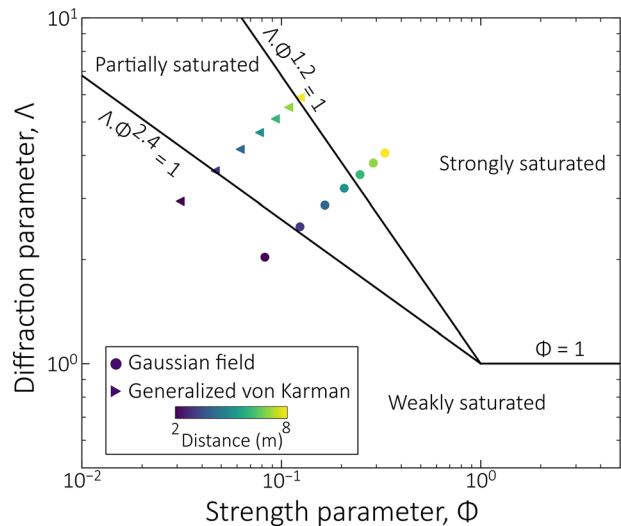


FIG. 6. (Color online)  $\Lambda - \Phi$  diagram with boundaries between the various scattering regimes in terms of strength and diffraction. Circles represent data at various distances, considering the Gaussian model characteristics ( $L_{\text{Gauss}}$  and  $\sigma_{\epsilon,\text{Gauss}}^2$ ), whereas triangles represent  $\Lambda$  and  $\Phi$  computed using the generalized von Karman model characteristics ( $L_{\text{vKarman},p=1/3}$  and  $\sigma_{\epsilon,\text{vKarman},p=1/3}^2$ , respectively). For each model, distances are sampled every 1 m between 2 and 8 m.

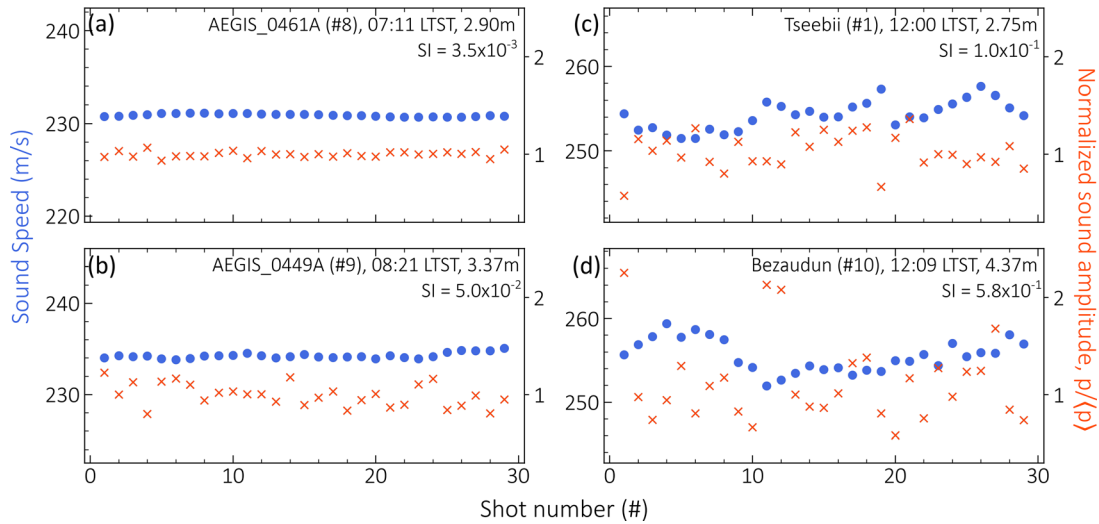


FIG. 7. (Color online) Evolution of the sound speed (blue circles, left axis) and the normalized sound amplitude (red crosses, right axis) acquired for four points at different local times and distances. The target name, its time of acquisition, and propagation distance are referenced within each panel. The left panels, (a) and (b), correspond to early morning acquisitions, whereas the right panels correspond to midday recordings. The associated values of SI are computed as described in Sec. II.

distance contributes to an increase in SI. Moreover, the travel time evolution follows the same trend but with lower variance, which supports the hypothesis that the amplitude scattering is mostly controlled by turbulence. As was performed in Sec. III, the statistics on SI are compared here with different turbulence spectra.

### A. Turbulence regimes

The comparison of SI and  $\sigma_\chi^2$  (the variance of the log-normal sound pressure) with theoretical models of propagation through thermal turbulence allows the turbulence regime applicable to Mars to be constrained (Blanc-Benon and Juvé, 1993). The relationship between SI and  $\sigma_\chi^2$  can be described following three solutions that depend on the strength of the perturbations.

For small perturbations, typically  $\sigma_\chi^2 \ll 1$ , the Rytov's method establishes a lognormal relationship between SI and  $\sigma_\chi^2$  (Tatarskii, 1961) such that

$$SI = \exp(4\sigma_\chi^2) - 1. \tag{10}$$

At the other extreme, in the case of strong perturbations ( $\sigma_\chi^2 \gg 1$ ), the asymptotic theory of Prokhorov *et al.* (1975) leads to an asymptotic solution:

$$SI = 1 + 1.22 (\sigma_\chi^2)^{-2/5}. \tag{11}$$

This relationship shows that SI does not increase infinitely but must reach a maximum before it decreases.

Between these two well-defined regimes of propagation, there are many data points for intermediate perturbations. Andrews *et al.* (1988) have proposed a phenomenological model, which is based on an *I-K* distribution, to connect both regimes such that

$$SI = \frac{2}{(1 + \rho)^2} \left( \frac{1}{2} + \frac{1 + \rho}{\alpha} \right). \tag{12}$$

The two parameters,  $\alpha$  and  $\rho$ , are determined using perturbation techniques for weak and strong turbulence (Andrews *et al.*, 1988):

$$\begin{cases} \alpha = 4.42 (\sigma_\chi^2)^{2/5}, \\ \rho = \frac{4.88}{9.84\alpha\sigma_\chi^2(1 + 1.97\sigma_\chi^2)}. \end{cases} \tag{13}$$

Figure 8 shows SI values as a function of  $\sigma_\chi^2$  for rocks at all distances acquired between 10:00 and 14:00 LTST, and

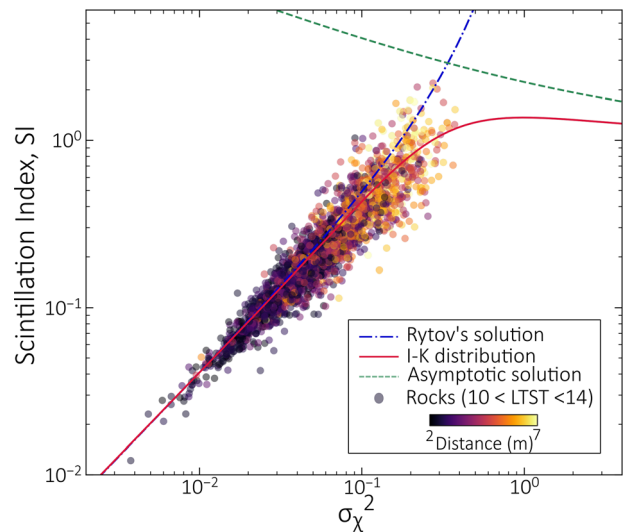


FIG. 8. (Color online) SI as a function of the variance of the lognormal of the sound amplitude ( $\sigma_\chi^2$ ) for all rocks acquired between 10:00 and 14:00 LTST. The propagation distance for each point is represented by the color-map (from black at 2 m to yellow at 7 m). Three models described in the main text, which correspond to weak (dashed-dotted blue), intermediate (solid red), and strong turbulence (dashed green) are displayed.

they are compared with the three aforementioned models. The match with the small perturbation model is very good over nearly 2 orders of magnitude in SI and  $\sigma_\chi^2$ . Deviation from the low-turbulence model occurs when SI > 0.3, which is in line with the literature (Blanc-Benon and Juvé, 1993). Most of the points resulting from a longer propagation distance ( $x > 7$  m, yellow points) better follow the *I-K* distribution and tend to fall in the intermediate regime. This confirms the observations in the Flatté plot (Fig. 6), where these long distance points are partly saturated. This also explains why these points deviate from the Iooss model for the variance of the travel time (see Fig. 4). Last, the saturation when SI values are leveling off is not reached.

### B. Variations with the propagation distance

As previously highlighted in Chide *et al.* (2023) and Figs. 7 and 8, SI varies with the propagation distance and its evolution law as a function of the distance allows to better constrain the turbulence spectrum at the origin of these variations.

Tatarskii (1961) has modeled the propagation of a spherical wave through a turbulent medium of power density,  $\phi(k)$ . For weak perturbations (following the Rytov's solution), the variance of the log-amplitude,  $\sigma_\chi^2$ , is given by (Tatarskii, 1961)

$$\sigma_\chi^2 = (2\pi)^2 k_0^2 \int_0^x dz \int_0^\infty \sin^2\left(\frac{z(x-z)}{2k_0x} k^2\right) \phi(k) k dk \quad (14)$$

for a receptor at a distance  $z = x$  from the source located at  $z = 0$ .  $k_0 = 2\pi f / c_0$  is the acoustic wavenumber estimated at the center frequency,  $f = 8$  kHz. The sine is a geometric factor. This double integral can be calculated for different power density profiles, numerically or analytically, as a function of  $x$ .

Equation (14), applied to the different fields introduced in Sec. III, leads to

- $\sigma_\chi^2 \propto x^{2.9}$  for a Gaussian field (analytical solution);
- $\sigma_\chi^2 \propto x^{1.83}$  for a pure Kolmogorov field (analytical solution);
- $\sigma_\chi^2 \propto x^{1.65}$  for a generalized von Karman field with  $p = 1/3$  (numerical solution); and
- $\sigma_\chi^2 \propto x^{1.25}$  for a generalized von Karman field with  $p = -1/6$  (numerical solution).

Figure 9 shows  $\sigma_\chi^2$  values as a function of the propagation distance for midday recordings (between 10:00 and 14:00 LTST). For points between 2 and 6 m (corresponding to the weak perturbation regime as per Fig. 2), data can be best fitted with  $\sigma_\chi^2 \propto x^{1.25}$ . This corresponds to a generalized von Karman field with  $p = -1/6$ .

### C. Synthesis of the results and discussions

In Sec. III, the turbulence characteristics for different temperature fluctuation fields were computed by comparing the variance of the travel time with Eq. (5). A summary of these parameters (outer scale of turbulence,  $L$ ; turbulence intensity,  $\sigma_\epsilon^2$ ; and temperature fluctuations,  $\sigma_T$ ) for each

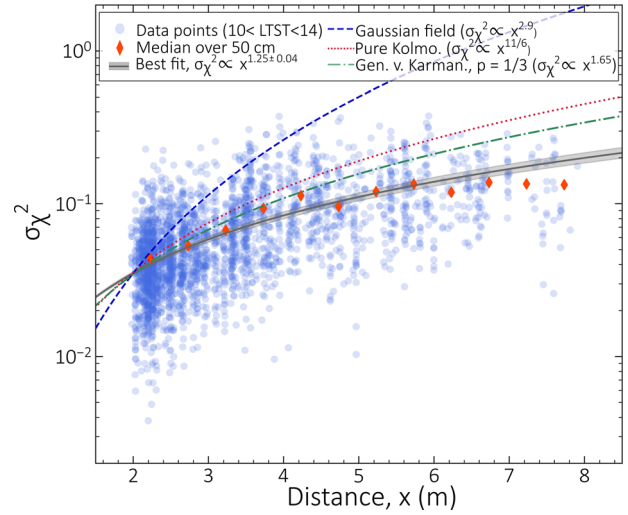


FIG. 9. (Color online) Variations of  $\sigma_\chi^2$  as a function of the propagation distance,  $x$ , for recordings between 10:00 and 14:00 LTST, all data; blue circles and mean over bins of 0.5 m, red diamonds. Expected models for a Gaussian field (dashed blue), pure Kolmogorov field (dotted red), and generalized von Karman field with  $p = 1/3$  (dashed-dotted green) are compared with the power law that best fits the data (solid gray).

fluctuation field tested is provided in Table I. However, this does not constrain the validity of one model over the others. Here, in Sec. IV, the evolution of the variance of the lognormal sound amplitude with distance tends to validate a generalized von Karman distribution with a parameter  $p = -1/6$ . Therefore, the acoustic dataset presented in this study, restricted to the midday period (10:00–14:00 LMST), is best represented by a turbulence field that has a power spectrum of  $\phi(k) \propto (1 + k^2 L^2)^{-4/3}$ , an outer scale of turbulence of  $L = 11$  cm and an intensity of  $\sigma_\epsilon^2 = 2 \times 10^{-3}$ , corresponding to a temperature fluctuation of 6 K over 9 s.

First, the sizes of the largest eddies found here are less than an order of magnitude larger than the theoretical end of the inertial regime, i.e., the inner scale of turbulence, which could be estimated for Mars at 2 cm (Maurice *et al.*, 2022; Petrosyan *et al.*, 2011). Note that the value for the inner scale of turbulence is not constant and may vary as a function of the local time and season. However, as no direct measurements are currently available, this value is taken as an order of magnitude. It tends to confirm that the inertial subrange on Mars is very small compared to its extent on Earth, as shown by previous *in situ* observations (Davy *et al.*, 2010; Tillman *et al.*, 1994). Then, the spectral slope of the power spectra found for the daytime data,  $-4/3$ , is shallower than the slope of  $-11/6$  currently predicted for temperature fluctuations by Kolmogorov theory for the inertial subrange [Eq. (6.26) in Ostashev and Wilson (2015)], reinforcing what is found on Mars for the temperature (de la Torre Juárez *et al.*, 2023) and wind velocity spectra (Viúdez-Moreiras *et al.*, 2022). In fact, Kolmogorov's theory of turbulence is based on the assumption of isotropic turbulence, which is not true for Mars or the Earth's atmospheric boundary layer. It supports Mars observations of the InSight pressure data (Banfield *et al.*, 2020; Temel

TABLE I. Summary of the midday acoustic turbulence characteristics computed in Sec. III for the four fluctuation fields considered in this study. It is compared with the results from Sec. IV, in the last column, which shows the agreement between the experimental evolution of  $\sigma_\chi^2$  and its expected evolution for each fluctuation field (see Fig. 9). The inner scale of turbulence,  $l_0$ , is not computed here and assumed to be 0.02 m.

Fluctuation field	Power spectrum $\phi(k)$	$L$ (cm)	$\sigma_\epsilon^2 \times 10^4$	$\sigma_T$ (K)	Agreement with Eq. (14)
Gaussian	$\exp(-k^2L^2)$	14	7.4	3	No
Pure Kolmogorov	$(k^2L^2)^{-11/6}$	N/A	N/A	N/A	No
Generalized von Karman ( $p = 1/3$ )	$(1 + k^2L^2)^{-11/6}$	23	9.7	4	No
Generalized von Karman ( $p = -1/6$ )	$(1 + k^2L^2)^{-4/3}$	11	20	6	Yes

*et al.*, 2022), which show a pressure spectrum that is flatter than expected. This may be explained by a strong stratification over the first few meters during the day, which introduces anisotropy, and a low thermal inertia of the ground, which induces strong thermal swings of the atmosphere and, thus, intermittency. It is also supported by the power spectra of temperature fluctuations recorded by the Perseverance MEDA weather station (de la Torre Juárez *et al.*, 2023), which show a different slope as a function of the time of day due to intermittent and sudden events (dust devils, convective cells, etc.). Another source of anisotropy comes from the inclined geometry of the experiment itself (Fig. 1), which means that the distribution of scales is not perfectly homogeneous along the propagation path. Indeed, this ground blocking effect damps the vertical fluctuations of the largest scales (Ostashev *et al.*, 2023). Therefore, the outer scale of turbulence,  $L$ , measured here is likely underestimated compared with a measurement in a free atmosphere. Moreover, in this study, temperature fluctuations have been considered to model the perturbation field,  $\epsilon$ . However, shear- and buoyancy-produced velocity fluctuations may also contribute to the perturbation field and, therefore, have a contribution to the effective power spectra of fluctuations [Eq. (7.30) in Ostashev and Wilson (2015)]. However, analyses of the Mars pressure and wind speed spectra (Murdoch *et al.*, 2023) have shown that these two quantities do not follow the Kolmogorov theory either. They tend to show shallower slopes, which are likely explained by anisotropy near the ground. The results presented in this study with temperature fluctuation spectrum confirm the observations presented by Murdoch *et al.* (2023). On a final note, the results presented are averaged over 800 Sols of data (more than one Martian year) with no distinction on the season or any meteorological event that might have happened during this period. However, Martian turbulence parameters computed here are likely to vary with the time of year or during specific weather, e.g., dust storm or gravity waves (Temel *et al.*, 2022). This will be the focus of an upcoming study.

## V. CONCLUSION AND PERSPECTIVES

In conclusion, the Perseverance rover is performing an original active acoustic experiment to infer, for the first time, the characteristics of the near-surface acoustic turbulence on Mars during the maximum of the convective period, which is between 10:00 and 14:00 LTST. Statistics on the travel time (mean value and variance) and amplitude

(SI) of the laser-induced acoustic waves are compared with an extensive theoretical work on the propagation of spherical waves in thermal turbulence (Blanc-Benon and Juvé, 1993; Iooss *et al.*, 2000; Tatarskii, 1961).

The study of the travel time as a function of the propagation distance helps to establish the key characteristics of the thermal turbulence (outer scale,  $L$ , and temperature standard deviation,  $\sigma_T$ ), comparing three different fluctuation fields (Gaussian, pure Kolmogorov, and generalized von Karman). All in all, as derived from this analysis, the daytime outer scale of turbulence of the Mars atmosphere ranges between 11 cm (smooth generalized von Karman) and 23 cm (for a standard generalized von Karman) with a temperature fluctuation that ranges between 3 K (Gaussian field) and 6 K (smooth generalized von Karman) over 9 s. Moreover, in the case of a Gaussian field, the variance of the travel times diverges from the linear Chernov model exactly where the density of occurrence of the first caustic reached its maximum. The study of the mean travel time itself shows that the acoustic waves travel, on average, faster than the mean speed of sound (fast path effect;  $-0.5\%$  at 6 m). Finally, using dimensionless strength and diffraction parameters (Flatté, 1983), it is revealed that the scattering of the acoustic signal begins to saturate beyond 7 m. A study of the SI helps to distinguish which of the tested fields best represents the data. Data match very well the theoretical model (Andrews *et al.*, 1988; Prokhorov *et al.*, 1975; Tatarskii, 1961): most of the recordings lie within a weak- to moderate-perturbation field of turbulence, also called the Rytov's solution. Considering the simplifying assumptions assumed in this study, a model of SI variation with distance (Ishimaru, 1978) favors a generalized von Karman spectrum with a shallower slope than the Kolmogorov cascade:  $\phi(k) \propto (1 + k^2L^2)^{-4/3}$ , where  $L = 11$  cm and  $\sigma_T = 6$  K. These values are within the ranges of temperature fluctuation probability density functions reported in de la Torre Juárez *et al.* (2023). This result is averaged over the first 800 Sols of the mission. Overall, by only considering thermal fluctuations, the agreement between the two independent datasets, travel time and scintillation, with respect to sound propagation models is quite good, and shows that the theory of acoustic wave propagation in random media is a promising tool to probe the turbulence near the surface of Mars. It also presents a new and interesting framework to adapt theoretical terrestrial models to Martian conditions.

To go further, the simplifying hypotheses used to perform this study should be investigated, especially to better determine

whether the contribution of the wind velocity fluctuations is important. Now that the shape of the turbulence spectrum has been estimated, this methodology should be applied at different times of the Martian year to highlight any change of the turbulence properties with season. In particular, acoustic data recorded during dust storms (Lemmon *et al.*, 2022) could help to validate if such conditions have an impact on the energy cascade (Temel *et al.*, 2022). This requires a good sampling on the propagation distance over a short period of time (typically 10 Sols) to fit the evolution of the SI. However, propagation distance is not evenly sampled during the mission as targets are usually selected for the geological rationale. This is even more the case when it comes to study the nocturnal conditions for which only a couple of recordings are available. It would be necessary to collect more nighttime data to further characterize the shear-induced turbulence observed at Jezero crater (Pla-García *et al.*, 2023) and detect the intermittent turbulence highlighted on InSight pressure data (Banfield *et al.*, 2020). For such purposes, a dedicated sound propagation campaign could be required. To complement this study, microphone recordings in passive mode (without any source other than atmospheric motions) give direct access to pressure fluctuations at the boundary between the inertial and dissipative regimes (Maurice *et al.*, 2022). Numerous 167 s long recordings, at all local times and even during the night, are currently acquired at 25 kHz. Their study will allow a better understanding of the inner scale of turbulence (i.e., the dissipation length) and its variations as a function of wind intensity, local time, and season. Last, the quantities that have just been calculated (spectral slope, intensity, and outer scale of turbulence) are related to fluctuations in refractivity index, that is, density fluctuations. Therefore, they can be used to parameterize these turbulence processes in numerical large eddy simulations, which cannot be resolved at such a small time scale.

**ACKNOWLEDGMENTS**

The authors thank the Mars2020 Science, operation, and engineering teams for their work to support the mission that has enabled the scientific research presented in this manuscript. This project was supported in the United States by the National Aeronautics and Space Administration’s Mars Exploration Program and in France is conducted under the authority of Centre National d’Etudes Spatiales. B.C. is supported by the Director’s Postdoctoral Fellowship from the Los Alamos National Laboratory, Grant No. 20210960PRD3. F.S. and S.S. are supported by German Aerospace Center. A.E.S. is supported by a Centre National d’Etudes Spatiales postdoctoral fellowship. The authors thank the three reviewers for their thorough reviews, which greatly improved the manuscript.

**AUTHOR DECLARATIONS**

**Conflict Interest**

The authors declare that they have no known competing financial interests or personal relationships that could have appeared to influence the work reported in this paper.

**DATA AVAILABILITY**

The data that support the findings of this study are openly available in the Planetary Data System under the SuperCam Archive Bundle in the SuperCam calibrated audio data collection.

**APPENDIX A: LASER PROPAGATION**

The propagation of electromagnetic signals through a turbulent atmosphere is affected by random fluctuations in its refractive index (Tatarskii, 1961). These fluctuations cause optical turbulence, called scintillation, of the laser beam that generates the acoustic wave used in this experiment. The Rytov approximation, which has been discussed for the propagation of acoustic waves in the case of a Kolmogorov energy cascade typically corresponding to the inertial regime (Tatarskii, 1961), also applies to the propagation of a coherent electromagnetic wave, namely, a laser beam:

$$SI_{laser} = 1.23 C_n^2 k_{laser}^{7/6} x^{11/6}, \tag{A1}$$

where  $x$  is the propagation distance, and  $k_{laser} = 2\pi/\lambda_{laser}$  is the wavenumber associated with the laser wavelength,  $\lambda_{laser} = 1 \mu\text{m}$ .  $C_n^2$  is the refractive index structure coefficient, a measure of the turbulence strength. There is extended literature on the measurement of this coefficient at ground level on Earth, e.g., Tunick (2003). It typically ranges from  $10^{-16} - 10^{-15}$  (negligible, too low turbulence),  $10^{-15} - 10^{-14}$  (weak turbulence) to  $10^{-13} - 10^{-12} \text{ m}^{-2/3}$  (strong turbulence). For a path length of  $x = 500 \text{ m}$ , Sprangle and Hafizi (2014) show that  $SI \simeq 0.1$  for weak turbulence and  $SI \simeq 1$  for strong turbulence. Laserna *et al.* (2009) report on a laser ablation study very similar to ours but at a long distance of 120 m. They observe scintillation due to small fluctuations in the refractive index of the atmosphere, especially outdoors.

Here, an estimate of  $C_n^2$  for the surface of Mars is provided. If  $n$  is the atmosphere refractive index for a perfect gas in the absence of humidity (Bean and Dutton, 1966), then

$$N = (n - 1) 10^6 = K \frac{P}{T}, \tag{A2}$$

where  $P$  and  $T$  are the pressure and temperature, respectively, and  $K$  is a constant that depends on the composition of the gas. At 1 bar and 273 K,  $N = 288$  for air (Bean and Dutton, 1966), hence,  $K = 77.6 \text{ K mbar}^{-1}$ . Mars atmosphere is mostly made of  $\text{CO}_2$  and for  $\text{CO}_2$ ,  $N = 442$  (Bideau-Mehu *et al.*, 1973), hence,  $K = 119.2 \text{ K mbar}^{-1}$ . Taking into account the difference in surface temperature between Mars and Earth (240 and 293 K, respectively) and the difference in pressure (610 Pa and 1013 hPa, respectively), we find that  $N_{\text{Earth}} \simeq 88 N_{\text{Mars}}$ : the refractive index of Mars atmosphere is much smaller than that of Earth. Next, following the formalism proposed by several authors (e.g., Tatarskii, 1961; Wu *et al.*, 2021), it has been shown that within the Earth’s atmosphere in the absence of relative humidity,

$$C_n^2 = a^2 L^{4/3} \left( 7.9 \times 10^{-5} \frac{P}{T^2} \right)^2 \left( \frac{\partial \theta}{\partial h} \right)^2, \quad (\text{A3})$$

where

$$\theta = T \left( \frac{1000}{P} \right)^{\mathcal{R}/C_p}, \quad (\text{A4})$$

where  $a^2 = 2.8$ , a universal constant (Ottersten, 1969).  $L$  is the outer scale of turbulence, which has been discussed in the main body of this article.  $h$  is the altitude above the surface.  $\theta$  is the potential temperature, which is conserved with respect to adiabatic displacements from a reference pressure [i.e., Eq. (A4)].  $\mathcal{R}$  is the gas constant and  $C_p$  is the molar isobaric heat capacity. Hence, the ratio  $\mathcal{R}/C_p = 0.258$  for air. Thus,  $C_n^2$  depends on the square of pressure (referred to 1 bar at the surface) and temperature, as well as the square of the air temperature gradient. The same formalism can be applied to the Martian atmosphere with a reference to 610 Pa at the surface and using the proportionality factor,  $K$ , above such that

$$C_n^2 = a^2 L^{4/3} \left( 1.2 \times 10^{-4} \frac{P}{T^2} \right)^2 \left( \frac{\partial \theta}{\partial h} \right)^2, \quad (\text{A5})$$

where

$$\theta = T \left( \frac{6.1}{P} \right)^{0.257} \quad (\text{A6})$$

on Mars. For the same outer scale of turbulence and the same gradient of potential temperature,  $C_n^2(\text{Mars}) \simeq 2 \cdot 10^{-4} C_n^2(\text{Earth})$ , mostly because of the pressure ratio.

Finally, assuming a maximum value of 30 K for the potential temperature gradient near the surface (Munguira et al., 2023),  $L_0 = 30$  cm, a pressure of 610 Pa, and a temperature 240 K, the laser scintillation ranges from  $10^{-7}$  to  $6 \times 10^{-4}$  for distances between 1 and 10 m. This is a negligible value compared to the SI values considered in this sound propagation experiment.

## APPENDIX B: TURBULENCE MODELS

In the body of this study, different turbulence models are tested: a Gaussian distribution and variants of the Kolmogorov distribution. The objective of this appendix is to calculate for each of these spectra: (i) the coefficients  $A_1$  and  $A_2$  that are necessary for the analysis of the mean and variance of travel times [Eqs. (4) and (5)] and (ii) the variations of the variance of the lognormal of the sound pressure,  $\sigma_x^2$ , as a function of the propagation distance,  $x$ , to support the variations of SI.

The covariance function,  $C(\vec{r})$ , at a location,  $\vec{r}$ , in space is the inverse 3D Fourier transform of the power density spectrum,  $\phi(k)$ , where  $k$  is the wavenumber of the vector,  $\vec{k}$ .

$$C(\vec{r}) = \int \int_{-\infty}^{\infty} \phi(\vec{k}) \exp(i\vec{k} \cdot \vec{r}) d\vec{k}. \quad (\text{B1})$$

It is assumed that random processes in the medium are statistically isotropic such that the covariance function does not depend on the direction of  $\vec{r}$  but only on its magnitude. In spherical coordinates,  $d\vec{k} = k^2 \sin \theta dk d\theta d\phi$ , and along the propagation axis,  $\vec{k} \cdot \vec{r} = kr \cos \theta$ . Then, for a homogeneous and isotropic distribution, it gives (Strohbehn, 1968)

$$C(r) = \frac{4\pi}{r} \int_0^{\infty} k \phi(k) \sin(kr) dk. \quad (\text{B2})$$

From  $C(r)$ , a standardized covariance,  $N(u)$ , can be derived [see, also, Eq. (3)]:

$$C_\epsilon = \sigma_\epsilon^2 N\left(\frac{z}{L}\right). \quad (\text{B3})$$

Therefore, for a power spectrum  $\phi(k)$ , we can derive  $C(r)$  and then  $N(u)$ . Power spectra do not need to be normalized, but it is set that  $N(0) = 1$ . Iooss et al. (2000) have shown that  $A_1$  and  $A_2$  parameters [Eqs. (4) and (5)] can be calculated from  $N(u)$  and its first derivative such that

$$A_1 = \int_0^{\infty} N(u) du, \quad \text{and} \quad A_2 = \int_0^{\infty} \frac{N'(u)}{u} du. \quad (\text{B4})$$

For a Gaussian spectrum, Eqs. (B2) and (B3) yield  $N(u) = \exp(-u^2)$ . Then, Eq. (B4) gives  $A_1 = \frac{1}{2}\pi$  and  $A_2 = -\sqrt{\pi}$ .

The Kolmogorov spectrum is not realistic as it increases continuously at low wavenumbers. Thus, it is not possible to derive a covariance function that can be normalized at zero, nor coefficients  $A_1$  and  $A_2$ .

For a generalized von Karman spectrum,  $\phi \propto (1 + \kappa^2 L^2)^{-p-3/2}$ , the associated covariance function [Eqs. (B2) and (B3)] is

$$N(u) = \frac{2^{-p+1}}{\Gamma(p)} u^p K_p(u), \quad (\text{B5})$$

where  $K_p$  is the modified Bessel function of second type of order  $p$ , and  $\Gamma$  is the gamma function. Then, we obtain

$$\begin{cases} A_1 = \sqrt{\pi} \frac{\Gamma(p+1/2)}{\Gamma(p)}, \\ A_2 = -\frac{\sqrt{\pi}}{2} \frac{\Gamma(p-1/2)}{\Gamma(p)}. \end{cases} \quad (\text{B6})$$

Note that Iooss et al. (2000) found a similar result but with a typo for  $A_2$ .

Alvarez-Llamas, C., Laserna, J., Moros, J., Purohit, P., García-Gómez, L., Angel, S., Bernardi, P., Bousquet, B., Cadu, A., Dauson, E., Forni, O., Fouchet, T., Gasnault, O., Jacob, X., Lacombe, G., Lanza, N., Larmat, C., Lasue, J., Lorenz, R., Meslin, P.-Y., Mimoun, D., Montmessin, F., Murdoch, N., Ollila, A., Pilleri, P., Randazzo, N., Reyes-Newell, A., Schröder, S., Stott, A., Cate, J. T., Udry, A., Vogt, D., Clegg, S., Cousin, A., Maurice, S., and Wiens, R. (2023). "The sound of geological targets on Mars from the absolute intensity of laser-induced sparks shock waves," *Spectrochim. Acta Part B: At. Spectrosc.* **205**, 106687.

Andrews, L. C., Phillips, R. L., and Shivamoggi, B. K. (1988). "Relations of the parameters of the  $I$ - $K$  distribution for irradiance fluctuations to physical parameters of the turbulence," *Appl. Opt.* **27**, 2150–2156.





- Lasue, J., Cousin, A., Meslin, P. Y., Mangold, N., Wiens, R. C., Berger, G., Dehouck, E., Forni, O., Goetz, W., Gasnault, O., Rapin, W., Schroeder, S., Ollila, A., Johnson, J., Le Mouélic, S., Maurice, S., Anderson, R., Blaney, D., Clark, B., Clegg, S. M., d'Uston, C., Fabre, C., Lanza, N., Madsen, M. B., Martin-Torres, J., Melikechi, N., Newsom, H., Sautter, V., and Zorzano, M. P. (2018). "Martian eolian dust probed by ChemCam." *Geophys. Res. Lett.* **45**(20), 10968–10977, <https://doi.org/10.1029/2018GL079210>.
- Lemmon, M. T., Smith, M. D., Viudez-Moreiras, D., de la Torre-Juarez, M., Vicente-Retortillo, A., Munguira, A., Sanchez-Lavega, A., Hueso, R., Martínez, G., Chide, B., Sullivan, R., Toledo, D., Tamppari, L., Bertrand, T., Bell, J. F., Newman, C., Baker, M., Banfield, D., Rodriguez-Manfredi, J. A., Maki, J. N., and Apestigue, V. (2022). "Dust, sand, and winds within an active Martian storm in Jezero crater." *Geophys. Res. Lett.* **49**(17), e2022GL100126, <https://doi.org/10.1029/2022GL100126>.
- Lorenz, R. D., Maurice, S., Chide, B., Mimoun, D., Stott, A., Murdoch, N., Giller, M., Jacob, X., Wiens, R. C., Montmessin, F., Grip, H., Tzanetos, T., Balam, B., Williams, N., Keennon, M., Langberg, S., Tyler, J., Bertrand, T., Brown, A., Randazzo, N., and Pipenberg, B. (2023). "The sounds of a helicopter on mars." *Planet. Space Sci.* **230**, 105684.
- Martins, L. G. N., Acevedo, O. C., Puhales, F. S., Degrazia, G. A., and Oliveira, P. E. S. (2021). "Vertical profiles of turbulence parameters in the thermal internal boundary layer." *Boundary-Layer Meteorol.* **179**(3), 423–446.
- Maurice, S., Chide, B., Murdoch, N., Lorenz, R. D., Mimoun, D., Wiens, R. C., Stott, A., Jacob, X., Bertrand, T., Montmessin, F., Lanza, N. L., Alvarez-Llamas, C., Angel, S. M., Aung, M., Balam, J., Beyssac, O., Cousin, A., Delory, G., Forni, O., Fouchet, T., Gasnault, O., Grip, H., Hecht, M., Hoffman, J., Laserna, J., Lasue, J., Maki, J., McClean, J., Meslin, P.-Y., Le Mouélic, S., Munguira, A., Newman, C. E., Rodríguez Manfredi, J. A., Moros, J., Ollila, A., Pilleri, P., Schröder, S., de la Torre Juárez, M., Tzanetos, T., Stack, K. M., Farley, K., Williford, K., and SuperCam team (2022). "In situ recording of Mars soundscape." *Nature* **605**(7911), 653–658.
- Maurice, S., Wiens, R. C., Bernardi, P., Caïs, P., Robinson, S., Nelson, T., Gasnault, O., Reess, J.-M., Deleuze, M., Rull, F., Manrique, J.-A., Abbaki, S., Anderson, R. B., André, Y., Angel, S. M., Arana, G., Battault, T., Beck, P., Benzerara, K., Bernard, S., Berthias, J.-P., Beyssac, O., Bonafous, M., Bousquet, B., Boutillier, M., Cadu, A., Castro, K., Chapron, F., Chide, B., Clark, K., Clavé, E., Clegg, S., Cloutis, E., Collin, C., Cordoba, E. C., Cousin, A., Dameury, J.-C., D'Anna, W., Daydou, Y., Debus, A., Deflores, L., Dehouck, E., Delapp, D., Santos, G. D. L., Donny, C., Doressoundiram, A., Dromart, G., Dubois, B., Dufour, A., Dupieux, M., Egan, M., Ervin, J., Fabre, C., Fau, A., Fischer, W., Forni, O., Fouchet, T., Frydenvang, J., Gauffre, S., Gauthier, M., Gharakanian, V., Gilard, O., Gontijo, I., Gonzalez, R., Granena, D., Grotzinger, J., Hassen-Khodja, R., Heim, M., Hello, Y., Hervet, G., Humeau, O., Jacob, X., Jacquino, S., Johnson, J. R., Kouach, D., Lacombe, G., Lanza, N., Lapauw, L., Laserna, J., Lasue, J., Deit, L. L., Mouélic, S. L., Comte, E. L., Lee, Q.-M., Legett, C., Leveille, R., Lewin, E., Leyrat, C., Lopez-Reyes, G., Lorenz, R., Lucero, B., Madariaga, J. M., Madsen, S., Madsen, M., Mangold, N., Manni, F., Mariscal, J.-F., Martinez-Frias, J., Mathieu, K., Mathon, R., McCabe, K. P., McConnochie, T., McLennan, S. M., Mekki, J., Melikechi, N., Meslin, P.-Y., Micheau, Y., Michel, Y., Michel, J. M., Mimoun, D., Misra, A., Montagnac, G., Montaron, C., Montmessin, F., Moros, J., Mousset, V., Morizet, Y., Murdoch, N., Newell, R. T., Newsom, H., Tuong, N. N., Ollila, A. M., Ortner, G., Oudda, L., Pares, L., Parisot, J., Parot, Y., Pérez, R., Pheav, D., Picot, L., Pilleri, P., Pilonget, C., Pinet, P., Pont, G., Poulet, F., Quantin-Nataf, C., Quartier, B., Rambaud, D., Rapin, W., Romano, P., Roucayrol, L., Royer, C., Ruellan, M., Sandoval, B. F., Sautter, V., Schoppers, M. J., Schröder, S., Seran, H.-C., Sharma, S. K., Sobron, P., Sodki, M., Sournac, A., Sridhar, V., Standarovskiy, D., Storms, S., Striebig, N., Tatat, M., Toplis, M., and Torre-Fdez, I. (2021). "The SuperCam instrument suite on the Mars 2020 rover: Science objectives and mast-unit description." *Space Sci. Rev.* **217**(3), 47.
- Mimoun, D., Cadu, A., Murdoch, N., Chide, B., Sournac, A., Parot, Y., Bernardi, P., Pilleri, P., Stott, A., Gillier, M., Sridhar, V., Maurice, S., Wiens, R., and SuperCam team (2023). "The Mars microphone onboard SuperCam." *Space Sci. Rev.* **219**(1), 5.
- Munguira, A., Hueso, R., Sánchez-Lavega, A., de la Torre-Juarez, M., Martínez, G. M., Newman, C. E., Sebastian, E., Lepinette, A., Vicente-Retortillo, A., Chide, B., Lemmon, M. T., Bertrand, T., Lorenz, R. D., Banfield, D., Gómez-Elvira, J., Martín-Soler, J., Navarro, S., Pla-García, J., Rodríguez-Manfredi, J. A., Romeral, J., Smith, M. D., and Torres, J. (2023). "Near surface atmospheric temperatures at Jezero from Mars 2020 MEDA measurements." *J. Geophys. Res. Planets* **128**(3), e2022JE007559, <https://doi.org/10.1029/2022JE007559>.
- Murdoch, N., Stott, A. E., Gillier, M., Hueso, R., Lemmon, M., Martínez, G., Apéstigue, V., Toledo, D., Lorenz, R. D., Chide, B., Munguira, A., Sánchez-Lavega, A., Vicente-Retortillo, A., Newman, C. E., Maurice, S., de la Torre Juárez, M., Bertrand, T., Banfield, D., Navarro, S., Marin, M., Torres, J., Gomez-Elvira, J., Jacob, X., Cadu, A., Sournac, A., Rodriguez-Manfredi, J. A., Wiens, R. C., and Mimoun, D. (2022). "The sound of a Martian dust devil." *Nat. Commun.* **13**(1), 7505.
- Murdoch, N., Stott, A. E., Mimoun, D., Pinot, B., Chatain, A., Spiga, A., Temel, O., Garcia, J. P., Onodera, K., Lorenz, R., Gillier, M., Newman, C., Garcia, R. F., Lange, L., and Banfield, D. (2023). "Investigating diurnal and seasonal turbulence variations of the Martian atmosphere using a spectral approach." *Planet. Sci. J.* **4**(11), 222.
- Obukhov, A. M. (1994). "Sound and light propagation in a weakly inhomogeneous atmosphere." *Waves Random Media* **4**(1), 9–19.
- Ostashev, V. E., and Wilson, D. K. (2015). *Acoustics in Moving Inhomogeneous Media* (CRC Press, Boca Raton, FL).
- Ostashev, V. E., and Wilson, D. K. (2017). "Strength and wave parameters for sound propagation in random media." *J. Acoust. Soc. Am.* **141**(3), 2079–2092.
- Ostashev, V. E., Wilson, D. K., and Hart, C. R. (2023). "Influence of ground blocking on the acoustic phase variance in a turbulent atmosphere." *J. Acoust. Soc. Am.* **154**(1), 346–360.
- Ottersten, H. (1969). "Mean vertical gradient of potential refractive index in turbulent mixing and radar detection of CAT." *Radio Sci.* **4**(12), 1247–1249, <https://doi.org/10.1029/RS004i012p01247>.
- Petrosyan, A., Galperin, B., Larsen, S. E., Lewis, S. R., Määttänen, A., Read, P. L., Renno, N., Rogberg, L. P. H. T., Savijärvi, H., Siili, T., Spiga, A., Toigo, A., and Vázquez, L. (2011). "The Martian atmospheric boundary layer." *Rev. Geophys.* **49**(3), RG3005, <https://doi.org/10.1029/2010RG000351>.
- Pla-García, J., Munguira, A., Rafkin, S., Newman, C., Bertrand, T., Martínez, G., Hueso, R., Sánchez-Lavega, A., del Río Gaztelurrutia, T., Stott, A., Murdoch, N., de la Torre Juárez, M., Lemmon, M., Chide, B., Viúdez-Moreiras, D., Savijärvi, H., Richardson, M., Marin, M., Sebastian, E., Lepinette-Malvitte, A., Mora, L., and Rodríguez-Manfredi, J. A. (2023). "Nocturnal turbulence at Jezero crater as determined from MEDA measurements and modeling." *J. Geophys. Res. Planets* **128**(8), e2022JE007607, <https://doi.org/10.1029/2022JE007607>.
- Prokhorov, A. M., Bunkin, F. V., Gochelashvili, K. S., and Shishov, V. I. (1975). "Laser irradiance propagation in turbulent media." *Proc. IEEE* **63**, 790–811.
- Read, P. L., Galperin, B., Larsen, S. E., Lewis, S. R., Määttänen, A., Petrosyan, A., Rennó, N., Savijärvi, H., Siili, T., Spiga, A., Toigo, A., and Vázquez, L. (2017). "The Martian planetary boundary layer." in *The Atmosphere and Climate of Mars* (Cambridge University Press, Cambridge, UK), pp. 172–202.
- Rodríguez-Manfredi, J. A., de la Torre Juárez, M., Sanchez-Lavega, A., Hueso, R., Martínez, G., Lemmon, M. T., Newman, C. E., Munguira, A., Hieta, M., Tamppari, L. K., Polkko, J., Toledo, D., Sebastian, E., Smith, M. D., Jaakonaho, I., Genzer, M., De Vicente-Retortillo, A., Viudez-Moreiras, D., Ramos, M., Saiz-Lopez, A., Lepinette, A., Wolff, M., Sullivan, R. J., Gomez-Elvira, J., Apestigue, V., Conrad, P. G., Del Rio-Gaztelurrutia, T., Murdoch, N., Arruego, I., Banfield, D., Boland, J., Brown, A. J., Ceballos, J., Dominguez-Pumar, M., Espejo, S., Fairén, A. G., Ferrandiz, R., Fischer, E., Garcia-Villadangos, M., Gimenez, S., Gomez-Gomez, F., Guzewich, S. D., Harri, A.-M., Jimenez, J. J., Jimenez, V., Mäkinen, T., Marin, M., Martin, C., Martin-Soler, J., Molina, A., Mora-Sotomayor, L., Navarro, S., Peinado, V., Perez-Grande, I., Pla-Garcia, J., Postigo, M., Prieto-Ballesteros, O., Rafkin, S. C. R., Richardson, M. I., Romeral, J., Romero, C., Savijärvi, H., Schofield, J. T., Torres, J., Urqui, R., and Zurita, S. (2023). "The diverse meteorology of Jezero crater over the first 250 Sols of perseverance on mars." *Nat. Geosci.* **16**(1), 19–28.
- Rytov, S. M., Kravtsov, Y. A., and Tatarskii, V. I. (1987). *Principles of Statistical Radiophysics 1. Elements of Random Process Theory*. (Springer, New York).

- Seel, F., Schröder, S., Vogt, D., Dietz, E., Hübers, H.-W., and Gensch, M. (2023). "Generation and evolution of laser-induced shock waves under Martian atmospheric conditions," *Icarus* **394**, 115405.
- Spiga, A. (2019). "The planetary boundary layer of Mars," in *Oxford Research Encyclopedia of Planetary Science* (Oxford University Press, New York).
- Sprangle, P., and Hafizi, B. (2014). "High-power, high-intensity laser propagation and interactions," *Phys. Plasmas* **21**(5), 055402.
- Stott, A. E., Murdoch, N., Gillier, M., Banfield, D., Bertrand, T., Chide, B., la Torre Juárez, M. D., Hueso, R., Lorenz, R., Martínez, G., Munguira, A., Sotomayor, L. M., Navarro, S., Newman, C., Pilleri, P., Pla-García, J., Rodríguez-Manfredi, J. A., Sánchez-Lavega, A., Smith, M., Moreiras, D. V., Williams, N., Maurice, S., Wiens, R. C., and Mimoun, D. (2023). "Wind and turbulence observations with the Mars microphone on perseverance," *J. Geophys. Res. Planets* **128**(5), e2022JE007547, <https://doi.org/10.1029/2022JE007547>.
- Strohbehn, J. (1968). "Line-of-sight wave propagation through the turbulent atmosphere," *Proc. IEEE* **56**(8), 1301–1318.
- Tatarskii, V. I. (1961). *Wave Propagation in Turbulent Medium* (McGraw-Hill, Berkshire, UK).
- Tatarskii, V. I. (1967). *The Effects of the Turbulent Atmosphere on Wave Propagation* (Israel Program for Scientific Translations, Jerusalem).
- Temel, O., Senel, C. B., Spiga, A., Murdoch, N., Banfield, D., and Karatekin, O. (2022). "Spectral analysis of the Martian atmospheric turbulence: InSight observations," *Geophys. Res. Lett.* **49**(15), e2022GL099388, <https://doi.org/10.1029/2022GL099388>.
- Tillman, J. E., Landberg, L., and Larsen, S. E. (1994). "The boundary layer of Mars: Fluxes, stability, turbulent spectra, and growth of the mixed layer," *J. Atmos. Sci.* **51**(12), 1709–1727.
- Tunick, A. (2003). "CN2 model to calculate the micrometeorological influences on the refractive index structure parameter," *Environ. Modell. Software* **18**, 165–171.
- Viúdez-Moreiras, D., de la Torre, M., Gómez-Elvira, J., Lorenz, R. D., Apéstigue, V., Guzewich, S., Mischna, M., Sullivan, R., Herkenhoff, K., Toledo, D., Lemmon, M., Smith, M., Newman, C. E., Sánchez-Lavega, A., Rodríguez-Manfredi, J. A., Richardson, M., Hueso, R., Harri, A. M., Tampari, L., Arruego, I., and Bell, J. (2022). "Winds at the Mars 2020 landing site. 2. Wind variability and turbulence," *J. Geophys. Res. Planets* **127**(12), e2022JE007523, <https://doi.org/10.1029/2022JE007523>.
- Vogt, D., Schröder, S., Frohmann, S., Hansen, P., Seel, F., Gensch, M., and Hübers, H.-W. (2022). "Spatiotemporal characterization of the laser-induced plasma plume in simulated Martian conditions," *Spectrochim. Acta Part B: At. Spectrosc.* **187**, 106326.
- White, B. S. (1984). "The stochastic caustic," *SIAM J. Appl. Math.* **44**(1), 127–149.
- Wiens, R. C., Maurice, S., Robinson, S. H., Nelson, A. E., Cais, P., Bernardi, P., Newell, R. T., Clegg, S., Sharma, S. K., Storms, S., Deming, J., Beckman, D., Ollila, A. M., Gasnault, O., Anderson, R. B., André, Y., Angel, S. M., Arana, G., Auden, E., Beck, P., Becker, J., Benzerara, K., Bernard, S., Beyssac, O., Borges, L., Bousquet, B., Boyd, K., Caffrey, M., Carlson, J., Castro, K., Celis, J., Chide, B., Clark, K., Cloutis, E., Cordoba, E. C., Cousin, A., Dale, M., Deflores, L., Delapp, D., Deleuze, M., Dirmeyer, M., Donny, C., Dromart, G., Duran, M. G., Egan, M., Ervin, J., Fabre, C., Fau, A., Fischer, W., Fouchet, T., Fresquez, R., Frydenvang, J., Gasway, D., Gontijo, I., Grotzinger, J., Jacob, X., Jacquino, S., Johnson, J. R., Klisiewicz, R. A., Lake, J., Lanza, N., Laserna, J., Lasue, J., Mouélic, S. L., Legett, C., Leveille, R., Lewin, E., Lopez-Reyes, G., Lorenz, R., Lorigny, E., Love, S. P., Lucero, B., Madariaga, J. M., Madsen, M., Madsen, S., Mangold, N., Manrique, J. A., Martínez, J. P., Martínez-Frias, J., McCabe, K. P., McConnochie, T. H., McGlown, J. M., McLennan, S. M., Melikechi, N., Meslin, P.-Y., Michel, J. M., Mimoun, D., Misra, A., Montagnac, G., Montmessin, F., Mousset, V., Murdoch, N., Newsom, H., Ott, L. A., Ousnamer, Z. R., Pares, L., Parot, Y., Pawluczuk, R., Peterson, C. G., Pilleri, P., Pinet, P., Pont, G., Poulet, F., Provost, C., Quertier, B., Quinn, H., Rapin, W., Reess, J.-M., Regan, A. H., Reyes-Newell, A. L., Romano, P. J., Royer, C., Rull, F., Sandoval, B., Sarrao, J. H., Sautter, V., Schoppers, M. J., Schröder, S., Seitz, D., Shepherd, T., Sobron, P., Dubois, B., Sridhar, V., Toplis, M. J., Torre-Fdez, I., Trettel, I. A., Underwood, M., Valdez, A., Valdez, J., Venhaus, D., and Willis, P. (2020). "The SuperCam instrument suite on the NASA Mars 2020 rover: Body unit and combined system tests," *Space Sci. Rev.* **217**(1), 4.
- Wilson, D. K. (2000). "A turbulence spectral model for sound propagation in the atmosphere that incorporates shear and buoyancy forcings," *J. Acoust. Soc. Am.* **108**(5), 2021–2038.
- Wilson, D. K., Brasseur, J. G., and Gilbert, K. E. (1999). "Acoustic scattering and the spectrum of atmospheric turbulence," *J. Acoust. Soc. Am.* **105**(1), 30–34.
- Wu, S., Wu, X., Su, C., Yang, Q., Xu, J., Luo, T., Huang, C., and Qing, C. (2021). "Reliable model to estimate the profile of the refractive index structure parameter ( $C_n^2$ ) and integrated astroclimatic parameters in the atmosphere," *Opt. Express* **29**(8), 12454–12470.
- Yuldashev, P. V., Ollivier, S., Karzova, M. M., Khokhlova, V. A., and Blanc-Benon, P. (2017). "Statistics of peak overpressure and shock steepness for linear and nonlinear  $N$ -wave propagation in a kinematic turbulence," *J. Acoust. Soc. Am.* **142**(6), 3402–3415.